

Thermal and Electrical Transport across a Magnetic Quantum Critical Point

Heike Pfau¹, Stefanie Hartmann^{1,*}, Ulrike Stockert¹, Peijie Sun^{1,**}, Stefan Lausberg¹, Manuel Brando¹, Sven Friedemann^{1,+}, Cornelius Krellner^{1,+}, Christoph Geibel¹, Steffen Wirth¹, Stefan Kirchner^{2,1}, Elihu Abrahams³, Qimiao Si⁴ and Frank Steglich¹

¹*Max Planck Institute for Chemical Physics of Solids, Nöthnitzer Str. 40, 01187 Dresden, Germany*

²*Max Planck Institute for the Physics of Complex Systems, Nöthnitzer Str. 38, 01187 Dresden, Germany*

³*Department of Physics and Astronomy, University of California Los Angeles, 405 Hilgard Avenue, Los Angeles, CA 90095, USA*

⁴*Department of Physics and Astronomy, Rice University, Houston, TX 77005, USA*

**present address: Leibniz Institute for Solid State and Materials Research, Helmholtz Str. 20, 01069 Dresden, Germany*

***present address: Institute of Physics, Chinese Academy of Sciences, Beijing 100190, China*

+present address: Cavendish Laboratory, University of Cambridge, J.J. Thompson Avenue, Cambridge, CB3 0HE, UK

A quantum critical point (QCP) arises at a continuous transition between competing phases at zero temperature. Collective excitations at magnetic QCPs give rise to metallic properties that strongly deviate from the expectations of Landau's Fermi liquid description[1], the standard theory of electron correlations in metals. Central to this theory is the notion of quasiparticles, electronic excitations which possess the quantum numbers of the bare electrons. Here we report measurements of thermal and electrical transport across the field-induced magnetic QCP in the heavy-fermion compound YbRh_2Si_2 [2, 3]. We show that the ratio of the thermal to electrical conductivities at the zero-temperature limit obeys the Wiedemann-Franz (WF) law above the critical field, B_c . This is also expected at $B < B_c$, where weak antiferromagnetic order and a Fermi liquid phase form below 0.07 K ($B = 0$). However, at the critical field the low-temperature

electrical conductivity suggests a non-Fermi-liquid ground state and exceeds the thermal conductivity by about 10%. This apparent violation of the WF law provides evidence for an unconventional type of QCP at which the fundamental concept of Landau quasiparticles breaks down [4–6]. These results imply that Landau quasiparticles break up, and that the origin of this disintegration is inelastic scattering associated with electronic quantum critical fluctuations. Our finding brings new insights into understanding deviations from Fermi-liquid behaviour frequently observed in various classes of correlated materials.

In metallic systems, continuously suppressing magnetic order gives rise to a QCP [7] and leads to non-Fermi-liquid behaviour [2, 8–11]. Whether quasiparticles persist near the QCP, however, is a fundamental open issue. An established means to probe the fate of the quasiparticles is to compare the thermal conductivity (κ) and electrical conductivity (σ). If quasiparticles are well defined, the WF law specifies the zero-temperature ($T = 0$) value of the Lorenz number $L \equiv \kappa/T\sigma$ to be $L_0 = (\pi k_B)^2/3e^2$. Except for superconductors [12], where the Lorenz ratio $L/L_0 = 0$, a violation of the WF law would constitute a direct evidence for physics beyond the Fermi liquid theory. L/L_0 becomes larger than one if there are additional carriers which contribute to the heat current but not to the charge current [13]. By contrast, $L/L_0 < 1$ at $T = 0$ implies a breakdown of Landau quasiparticles.

Heavy-fermion metals are prototype systems for antiferromagnetic (AF) QCPs. These rare-earth or actinide-based intermetallics contain both f -derived localised magnetic moments and itinerant (spd) conduction electrons, whose entanglement gives rise to the Kondo effect and the concomitant composite quasiparticles with huge effective mass. In these materials, two types of QCPs have been highlighted. The spin-density-wave based theory relies on the fluctuations of the AF order parameter [14–16]. Here, the main part of the Fermi surface remains unaffected by the critical fluctuations, leaving the quasiparticles intact. In a related picture [17], all states near the Fermi surface are influenced by quantum critical fluctuations. At an unconventional type of QCP, a breakdown of the Kondo entanglement disintegrates all the heavy quasiparticles [4–6]. Neutron scattering and magnetic measurements [18] in $\text{CeCu}_{6-x}\text{Au}_x$, as well as de Haas-van Alphen [19] and thermodynamic and transport [20] measurements in CeRhIn_5 have been interpreted in terms of a local Kondo-breakdown QCP [4, 5]. In YbRh_2Si_2 , the weak AF order is continuously suppressed by a tiny magnetic field [2, 3, 21]. Electrical transport and thermodynamic measurements have

revealed multiple vanishing energy scales [22] and a discontinuity of the Fermi surface across the QCP [23, 24]. These materials provide a setting to characterize the quasiparticles near the AF QCP.

We focus on YbRh_2Si_2 , in order to take advantage of the understanding of its Fermi surface [23, 24]. Fig. 1 displays the overall T - B phase diagram (a) and the thermal conductivity below 12 K (b). At $B = 0$, the compound orders antiferromagnetically at $T_N = 0.07$ K. Increasing B to its critical value $B_c \approx 0.06$ T (\perp c) continuously suppresses T_N to zero, reaching the QCP. Below T_{FL} the paramagnetic phase at $B > B_c$ is a heavy Fermi liquid [3], in which the Fermi surface is large as a result of the Kondo effect. However, in the AF phase ($B < B_c$), also a mass-enhanced Fermi liquid [3], the Fermi surface is small, without incorporating the f -electrons [23, 24]. The $T^*(B)$ line defines a crossover of the Fermi surface as a function of the control parameter B , and terminates at $B = B_c$ as $T \rightarrow 0$. Upon cooling, the field range of quantum critical behaviour shrinks to $B = B_c$ in the $T = 0$ limit, whereas a Fermi-liquid ground state exists on either side of the QCP. The QCP is clearly identified by an asymptotic ($T \rightarrow 0$) linear temperature dependence of the electrical resistivity, independent of sample quality [21, 22]. In addition, the width of the T^* crossover is proportional to T , extrapolating to a sharp jump of the Fermi surface at $T = 0$ (Ref. 24). While these measurements prove the existence of two different states on either side of the QCP, they left open the nature of not only the electronic excitations in the quantum critical regime but also the dynamical processes underlying the Kondo breakdown.

A previous study of the thermal and electrical transport in the quasi-two-dimensional heavy-fermion metal CeCoIn_5 [25], in which a magnetic QCP is suspected [26] but not identified, found that the WF law is violated ($L/L_0 \approx 0.8$ as $T \rightarrow 0$) for c -axis transport but obeyed for in-plane transport. These results were discussed in terms of putative strongly anisotropic critical fluctuations, although how spin fluctuations may invalidate the WF law was left as an open question. Combined thermal and electrical transport has also been studied near the QCP of ZrZn_2 , which is considered a canonical ferromagnetic-spin-fluctuation system [27]. Although the two transport quantities in ZrZn_2 have different temperature dependencies, with $L/L_0 < 1$, their extrapolated $T = 0$ limits satisfy the WF law.

YbRh_2Si_2 provides a unique opportunity to study the fate of Landau quasiparticles at QCPs beyond the spin-fluctuation description and, likewise, the nature of the critical fluctu-

ations associated with the Kondo breakdown. The compound is also advantageous because superconductivity is absent down to at least 0.01 K (Ref. [21]), unlike the case of CeCoIn₅. This not only exposes the properties in the immediate vicinity of the AF QCP but also facilitates the characterization of the quasiparticles through the Lorenz ratio. YbRh₂Si₂ is a magnetically anisotropic metal; the possibility of quasi-two-dimensional transport necessitates the usage of in-plane transport to probe any quasiparticle breakdown [28]. The present study will therefore focus on the thermal and electrical transport within the tetragonal plane.

The thermal conductivity $\kappa(T)$ was measured between 0.025 K and 12 K and is shown in Fig. 1b for $B = 0$. For comparison, $\kappa_{\text{WF}}(T) \equiv L_0 T / \rho(T)$ was calculated from the measured electrical resistivity $\rho(T)$ and is also presented. Above 4 K, $\kappa(T)$ exceeds $\kappa_{\text{WF}}(T)$ due to the contribution of phonons to the heat transport, $\kappa_{\text{ph}}(T)$, see Supplementary Information (SI). Below 4 K, $\kappa_{\text{ph}}(T)$ is suppressed, and $\kappa(T)$ becomes smaller than $\kappa_{\text{WF}}(T)$ down to about 0.035 K and somewhat larger at even lower temperatures (Fig. 1a).

In order to investigate the WF law, we extrapolate the Lorenz ratio $L(T)/L_0 \equiv \rho(T)/w(T)$ to $T = 0$. Because a QCP is a singular point in the phase diagram, and given that there are temperature scales that vary as a function of the control parameter and vanish at the QCP, the combination of isofield and isothermal scans is crucial for the extrapolation (Sec. VI, SI).

Figure 2 depicts the low-temperature behaviour of both the electrical resistivity $\rho(T)$ and thermal resistivity $w(T) = L_0 T / \kappa(T)$ at zero field, $B = 0.06 \text{ T} \approx B_c$ and $B > B_c$. Here $w(T)$ has the same unit as $\rho(T)$. Similar results at other magnetic fields are given in Fig. S4 of SI. This comparison shows that $w(T)$ exceeds $\rho(T)$ over a wide range of temperature and field. Figures 3a,b and c,d display, respectively, the difference $w(T) - \rho(T)$ and the Lorenz ratio for the data shown in Figs. 2a–d. Corresponding plots for the data shown in Fig. S4 are presented in Figs. S5a,b and c,d.

Below $T = 0.15 \text{ K}$, at $B \geq 0.6 \text{ T}$, $w(T) = \rho(T)$ within the experimental resolution. This is illustrated for $B = 1 \text{ T}$ in Fig. 3b which shows that $w(T) - \rho(T)$ approaches zero in this range of T and B , and in Fig. 3d, which demonstrates that $L(T)/L_0 = 1$ within the experimental error. In this high-field range, both $\Delta\rho(T) = [\rho(T) - \rho_0] \propto T^2$ and $[w(T) - w_0] \propto T^2$ below the Fermi-liquid crossover temperature, marked by arrows in Fig. 2 and Fig. S4. Here, ρ_0 and w_0 are the residual ($T \rightarrow 0$) electrical and thermal resistivities, which are identical within about 1%. These results establish the validity of the WF law in the Fermi-liquid

phase for $B \geq 0.6$ T. For $0.2 \text{ T} \leq B \leq 0.6 \text{ T}$, the results shown in Figs. 2c and S4d–f suggest similar Fermi-liquid behaviour at lower temperatures.

The system is in the quantum critical regime [21] at $B = 0$ and $T \gtrsim 0.1$ K, where $w(T) > \rho(T)$. Both $\rho(T)$ and $w(T)$ decrease linearly with temperature below about 0.3 K which allows extrapolating the quantum critical behaviour of $\rho(T)$ and $w(T)$ to the $T = 0$ limit, giving $w_0 > \rho_0$. This is shown in Fig. 3a (dashed line) for $w(T) - \rho(T)$, which is about $0.17 \mu\Omega \text{ cm}$ at $T = 0$, and in Fig. 3c for $L(T)/L_0$, where the corresponding extrapolation (dashed line) yields about 0.9. Our extrapolation follows path C_1 (Fig. S8a, SI).

Upon cooling in zero field, $\rho(T)$ drops at the Néel transition [3] into the AF phase, reflecting the freezing out of spin-disorder scattering. Below T_N , $\rho(T)$ exhibits a Fermi-liquid T^2 dependence (Ref. [3]). We observe a drop in $w(T)$ as well; it starts already at $T \approx 0.1$ K (Fig. 2a). Furthermore, we find that $w(T) - \rho(T)$ below $T = 0.033$ K becomes negative (Fig. 3a), and L/L_0 exceeds one (Fig. 3c). An upturn of $L(T)/L_0$ just below T_N was also observed in Ref. [29] down to 0.05 K, where $L(T)/L_0$ is still below one but appears to extrapolate to one as $T \rightarrow 0$. Our observation of $L(T)/L_0 > 1$ below $T = 0.033$ K clearly shows that the thermal transport is not entirely due to electronic-quasiparticle transport, as concluded in Ref. [29]. Instead, the Fermi-liquid-type electronic transport is masked by that of an additional heat channel. In the SI we demonstrate that the additional thermal conductivity is due to AF magnons; this magnon contribution will vanish in the $T = 0$ limit, as is inferred from the specific-heat data [21] measured down to 0.018 K (see SI). Therefore, at $B = 0$ the WF law is expected to hold in the $T = 0$ limit.

At $B = 0.06 \text{ T} \approx B_c$, $\rho(T)$ is linear below 0.12 K down to the lowest measured temperature, as is $w(T)$ below about 0.2 K (Fig. 2b). At $T \approx 0.07$ K, $w(T)$ shows a downturn which is similar to, though considerably weaker than, that at $B = 0$ which sets in at higher temperature (Fig. 2a). We interpret this feature as the contribution of overdamped magnons in the paramagnetic regime above the reduced T_N , see SI; as in the case of $B = 0$, this magnetic contribution is expected to vanish in the $T \rightarrow 0$ limit. Extrapolating the T -linear electrical resistivity and the *electronic* thermal resistivity, which is also linear in T between 0.07 – 0.2 K, to $T = 0$ we find $(w_0 - \rho_0) > 0$ and $L(T \rightarrow 0)/L_0 < 1$, similar to the behaviour at $B = 0$ (Figs. 3a, c). Here, our extrapolation is taken near the path C (Fig. S8a, SI).

These results provide an overall picture that can be placed in the context of the phase diagram of Fig. 1a. For fields sufficiently above the critical field B_c , the WF law is obeyed

at low temperatures. At the same time, the data at $B = 0$ can be interpreted as validating the WF law in the $T = 0$ limit, *i.e.*, in the AF ground state. The validity of the WF law at magnetic fields away from B_c and for sufficiently low temperatures is consistent with a field-induced continuous quantum phase transition between two Fermi liquids with, respectively, small and large Fermi surfaces, which has been inferred from magnetotransport and thermodynamic measurements [22–24]. In contrast, the data in the paramagnetic quantum critical regime are extrapolated to a $T = 0$ limit that violates the WF law.

The isothermal field dependence $L(B)/L_0$ further clarifies these results. This is given in Fig. 3e, which shows a shallow minimum near a field that tracks the $T^*(B)$ line in Fig. 1a. The minimum narrows as temperature is reduced and extrapolates, as $T \rightarrow 0$, to an abrupt dip at $B = B_c$ (see SI); the extrapolated $T = 0$ value at that point is about 0.9 (*cf.* Fig. 3c). The systematic evolution of L/L_0 versus B and T provides evidence for the intrinsic nature of the apparent violation of the WF law in YbRh_2Si_2 .

Our findings shed considerable new light on the dynamical electronic processes occurring at the QCP. Quasiparticles disintegrate at a Kondo-breakdown QCP, as illustrated in Fig. 4. The large Fermi surface incorporates both the conduction electrons and delocalized f -electrons, while the small Fermi surface involves only the conduction electrons. Because the quantum phase transition is continuous, this change of the Fermi surface must result from inelastic processes that operate near the QCP. Such dynamical processes must be electronic, extending to zero energy when the system is precisely at the QCP. Correspondingly, the quasiparticle residue of the large Fermi surface, Z_L , and that of the small Fermi surface, Z_S , must reach zero as the QCP is approached from the paramagnetic and AF sides, respectively. At the critical value of the control parameter, they satisfy dynamical scaling:

$$\begin{aligned} Z_L(\mathbf{k}_F^L, T, \omega) &= a_L T^\alpha \varphi_L(\omega/T), \\ Z_S(\mathbf{k}_F^S, T, \omega) &= a_S T^\beta \varphi_S(\omega/T). \end{aligned} \tag{1}$$

These scaling forms of Z_L and Z_S capture the physics of the critical Kondo breakdown. The latter arises from the dynamical competition between RKKY and Kondo interactions which, respectively, promote small and large Fermi surfaces. The resulting critical fluctuations between the small and large Fermi surfaces amount to quantum critical inelastic scatterings for the electronic heat carriers, which lead to $L/L_0 < 1$ in the quantum-critical region. The vanishing quasiparticle weights, Z_L and Z_S , imply that such quantum fluctuations and

the concomitant fluctuating Fermi surfaces persist at the QCP, thereby making it natural for $L/L_0 < 1$ even in the $T = 0$ limit. In this way, our observation provides evidence for electronic quantum critical fluctuations which are naturally associated with the abrupt reconstruction of the Fermi surface.

Our study is to be contrasted with those that feature extra charge-neutral fermionic heat carriers. For example, over the intermediate temperature range that corresponds to the quasi-one-dimensional case of the “purple bronze” $\text{Li}_{0.9}\text{Mo}_6\text{O}_{17}$, one expects spin-charge separation. The chargeless spinons, which contribute to the heat conductivity, should give rise to $L/L_0 > 1$, and this is indeed observed [13]. In our case, the non-Fermi-liquid excitations carry both charge and heat currents and are subject to inelastic scatterings from quantum critical electronic fluctuations. As discussed in Sec. VI, SI, this leads to a Lorenz ratio less than one. Because it reflects the different degrees to which non-Umklapp processes contribute to the electrical and heat resistivities, the deviation in this case is expected to be more modest; this is consistent with the 10% effect observed here.

Our results indicate that a breakdown of Landau quasiparticles accompanies the vanishing of a quantum critical energy scale, $T^*(B)$, in YbRh_2Si_2 . This linkage between the emergence of non-Fermi-liquid excitations and vanishing of energy scales provides a tantalizing connection between quantum critical heavy-fermion metals and the high- T_c cuprates near optimal doping, where the pseudogap energy scale collapses and Fermi-liquid quasiparticles are destroyed over the entire Fermi surface [30].

Methods

The samples used in this work belong to the same batch and have been well characterized previously [3, 21]. Thermal and electrical transport coefficients were obtained from the same rectangular-shaped ($4.2 \times 0.5 \times 0.1 \text{ mm}^3$) single crystal (sample 1) with the same contact geometry. This allows a reliable determination of the Lorenz ratio $L(T)/L_0 = \rho(T)/w(T)$, since the geometry factor l/A cancels out, where l and A are the length and the cross-section of the sample, respectively (*cf.* SI). Additional measurements of the electrical resistivity were performed on a second single crystal from the same batch, but with different geometry factor (sample 2). As described in SI, the measured resistivity values could perfectly be rescaled by a factor 1.25 ± 0.03 and corrected by a difference in residual resistivity of $0.22 \mu\Omega\text{cm}$. Heat and charge currents as well as the magnetic field were applied within the basal tetragonal plane.

However, we did not consider the distinction between the [100] and the [110] directions within the basal plane. The parallel orientation of the magnetic field, supplied by a superconducting solenoid, to the heat and charge flow allows to neglect the contributions of transverse effects (Nernst and electrical/thermal Hall effects) in all measurements.

-
- [1] Landau, L. D. The theory of a Fermi liquid. *Sov. Phys. JETP* **6**, 920-925 (1957).
 - [2] Trovarelli, O. *et al.* YbRh₂Si₂: Pronounced non-Fermi-liquid effects above a low-lying magnetic phase transition. *Phys. Rev. Lett.* **85**, 626–629 (2000).
 - [3] Gegenwart, P. *et al.* Magnetic-field induced quantum critical point in YbRh₂Si₂. *Phys. Rev. Lett.* **89**, 056402 (2002).
 - [4] Si, Q., Rabello, S., Ingersent, K. & Smith, J. L. Locally critical quantum phase transitions in strongly correlated metals. *Nature* **413**, 804-808 (2001).
 - [5] Coleman, P., Pépin, C., Si, Q. & Ramazashvili, R. How do Fermi liquids get heavy and die? *J. Phys.: Condens. Matter* **13**, R723-R738 (2001).
 - [6] Senthil, T., Vojta, M. & Sachdev, S. Weak magnetism and non-Fermi liquids near heavy-fermion critical points. *Phys. Rev. B* **69**, 035111 (2004).
 - [7] Schofield, A. J. Quantum criticality and novel phases: Summary and outlook. *Phys. Status Solidi B* **247**, 563-569 (2010).
 - [8] Löhneysen, H. v. *et al.* Non-Fermi-liquid behavior in a heavy-fermion alloy at a magnetic instability. *Phys. Rev. Lett.* **72**, 3262-3265 (1994).
 - [9] Aronson, M. C. *et al.* Non-Fermi-liquid scaling of the magnetic response in UCu_{5-x}Pd_x ($x = 1, 1.5$). *Phys. Rev. Lett.* **75**, 725-728 (1995).
 - [10] Mathur, N. D. *et al.* Magnetically mediated superconductivity in heavy fermion compounds. *Nature* **394**, 39-43 (1998).
 - [11] Grigera, S. A. *et al.* Magnetic field-tuned quantum criticality in the metallic ruthenate Sr₃Ru₂O₇. *Science* **294**, 329-332 (2001).
 - [12] Einstein, A. Theoretical remark on the superconductivity of metals. arXiv:physics/051025 (translated from *Gedenkboek aangeb. aan H. Kamerlingh Onnes*, Leiden 1922).
 - [13] Wakeham, N. *et al.* Gross violation of the Wiedemann-Franz law in a quasi-one-dimensional conductor. *Nature Commun.* **2**, 396 (2011).

- [14] Hertz, J. A. Quantum critical phenomena. *Phys. Rev. B* **14**, 1165-1184 (1976).
- [15] Moriya, T. *Spin fluctuations in itinerant electron magnetism* (Springer, Berlin, 1985).
- [16] Millis, A. J. Effect of a nonzero temperature on quantum critical points in itinerant fermion systems. *Phys. Rev. B* **48**, 7183-7196 (1993).
- [17] Wölfle, P. & Abrahams, E. Quasiparticles beyond the Fermi liquid and heavy fermion criticality. *Phys. Rev. B* **84**, R041101 (2011).
- [18] Schröder, A. *et al.* Onset of antiferromagnetism in heavy-fermion metals. *Nature* **407**, 351-355 (2000).
- [19] Shishido, H., Settai, R., Harima, H. & Onuki, Y. A change of the Fermi surface at a critical pressure in CeRhIn₅: dHvA study under pressure. *J. Phys. Soc. Jpn.* **74**, 1103–1106 (2005).
- [20] Park, T. *et al.* Hidden magnetism and quantum criticality in the heavy fermion superconductor CeRhIn₅. *Nature* **440**, 65–68 (2006).
- [21] Custers, J. *et al.* The break-up of heavy electrons at a quantum critical point. *Nature* **424**, 524–527 (2003).
- [22] Gegenwart, P., Si, Q. & Steglich F. Quantum criticality in heavy-fermion metals. *Nature Phys.* **4**, 186-197 (2008).
- [23] Paschen, S. *et al.* Hall effect evolution at a heavy fermion quantum critical point. *Nature* **432**, 881-885 (2004).
- [24] Friedemann, S. *et al.* Fermi-surface collapse and dynamical scaling near a quantum critical point. *Proc. Natl. Acad. Sci. USA* **107**, 14547-14551 (2010).
- [25] Tanatar, M. A., Paglione J., Petrovic, C. & Taillefer L. Anisotropic violation of the Wiedemann-Franz law at a quantum critical point. *Science* **316**, 1320-1322 (2007).
- [26] Zaun, S. *et al.* Towards the identification of a quantum critical line in the (p, B) phase diagram of CeCoIn₅ with thermal-expansion measurements. *Phys. Rev. Lett.* **106**, 087003 (2011).
- [27] Smith R. P. *et al.* Marginal breakdown of the Fermi-liquid state on the border of metallic ferromagnetism. *Nature* **455**, 1220-1223 (2008).
- [28] Smith, M. F. & McKenzie, R. H. Apparent violation of the Wiedemann-Franz law near a magnetic field tuned metal-antiferromagnetic quantum critical point. *Phys. Rev. Lett.* **101**, 266403 (2008).
- [29] Tomokuni, K. *et al.* Thermal transport properties and quantum criticality of heavy fermion YbRh₂Si₂. *J. Phys. Soc. Jpn.* **80**, SA096 (2011).

- [30] Casey, P. A., Koralek, J. D., Plumb, N. C., Dessau, D. S. & Anderson, P. W. Accurate theoretical fits to laser-excited photoemission spectra in the normal phase of high-temperature superconductors. *Nature Phys.* **4**, 210-212 (2008).

Supplementary Information accompanies the paper on www.nature.com/nature.

Acknowledgements We thank P. Coleman, R. Daou, P. Gegenwart, N. E. Hussey, K. Ingersent, G. Kotliar, A. P. Mackenzie, H. von Löhneysen, J. Schmalian, A. J. Schofield, T. Senthil, S. Shastry, and Z. Tešanovic for useful discussions. The work has in part been supported by the DFG Research Unit 960 “Quantum Phase Transitions”, NSF Grant DMR-1006985 and the Robert A. Welch Foundation Grant No. C-1411. E. A., S. K., Q. S. and F. S. acknowledge the support in part by the National Science Foundation under Grant No. 1066293 and the hospitality of the Aspen Center for Physics.

Author contributions All authors contributed substantially to this work.

Author information Reprints and permissions information is available at www.nature.com/reprints. The authors declare no competing financial interests. Readers are welcome to comment on the online version of this article at www.nature.com/nature. Correspondence and requests for materials should be addressed to F. S. (steglich@cpfs.mpg.de).

FIG. 1: **Phase diagram and thermal conductivity of YbRh₂Si₂.** **a**, Temperature-magnetic-field phase diagram, indicating the antiferromagnetic phase (AF) boundary (T_N , solid line) and the crossovers between non-Fermi-liquid and Fermi-liquid (FL) regimes (T_{FL} , dashed line) as well as between small and large Fermi surfaces (T^* , double-dashed line). The crossover width at T^* is proportional to temperature (shaded region) (from [24]). The magnetic field, B , was applied within the basal tetragonal, easy magnetic plane, $\perp c$. Arrows indicate fields at which combined thermal and electrical transport measurements were performed (Figs. 2a-c). The WF law is strictly defined only in the $T = 0$ limit and is expected to describe the electronic transport of a Fermi liquid. This is illustrated in the low- T transport properties of the field-induced paramagnetic phase, $B > B_c$ (Figs. 2c,d). It is also expected in the AF phase, $B < B_c$: Here, at finite temperature the electronic thermal conductivity, κ_{el} , is masked by a contribution due to magnons, κ_m (see text). However, as $T \rightarrow 0$, κ_m vanishes such that the heat transport is purely electronic, and the WF law is valid. **b**, Thermal conductivity, κ , as a function of temperature, T , at zero field. The solid line displaying $\kappa_{WF}(T) = L_0 T / \rho(T)$ was obtained under the assumption of the WF law to hold in the whole range of temperatures $T \leq 12$ K; here, $\rho(T)$ is the electrical resistivity and $L_0 = 1/3(\pi k_B/e)^2$ Sommerfeld's constant. The dashed line shows the phonon contribution $\kappa_{ph}(T)$, as discussed in the Supplementary Information. Inset: same data below $T = 0.1$ K.

FIG. 2: Thermal and electrical resistivity curves at low temperatures. Thermal resistivity $w(T) = L_0 T / \kappa(T)$ and electrical resistivity $\rho(T)$ below $T = 0.5$ K for $B = 0$ **a**, 0.06 T **b**, 0.3 T **c** and 1 T **d**, $B \perp c$. Arrows in **c** and **d** indicate the crossover to Fermi-liquid behaviour (from Fig. 1a). Because T_N is very low (0.07 K), it is an experimental challenge to elucidate the intrinsic behaviour of the thermal transport in the AF regime. We have therefore made special efforts to not only extend the heat-transport measurements at $B = 0$ down to temperatures as low as 0.025 K, but also to reduce the statistical error of the data by performing substantially more temperature scans than at finite fields. The extrapolation specified by the dashed lines in **a** and **b** corresponds to the trajectory C_1 and one close to C , respectively, of Fig. S8a, SI. Representative error bars reflecting the standard deviation are shown for a few selected temperatures.

FIG. 3: Violation/validity of the Wiedemann-Franz law at $B \approx B_c/B > B_c$. **a**, Difference $(w - \rho)$ vs T at $B = 0$ and 0.06 T as well as **b** 0.3 T and 1 T. **c**, **d**, Lorenz ratio $L/L_0 = \rho/w$ vs T for the same fields as in **a**, **b**. Within the experimental uncertainty, the validity of the Wiedemann-Franz law is found below $T \approx 0.15$ K for $B = 1$ T and is anticipated at lower temperature for $B \geq 0.3$ T **b**, **d**. Dashed lines in **a**, **c** indicate T -linear behaviour of both $w(T)$ and $\rho(T)$ in the paramagnetic non-Fermi-liquid regime. For $B = 0$, the onset of the deviation from quantum critical behaviour (dashed lines in **a** and **c**) seems to occur at about 0.07 K, almost exactly where the corresponding feature becomes visible at $B = 0.06$ T, too. This is in striking contrast to Fig. 2a, showing that the deviation in the $w(T)$ data for $B = 0$ sets in already at $T \approx 0.1$ K. The reason for this seeming discrepancy lies in the pronounced drop of the electrical resistivity at $T_N = 0.07$ K (Fig. 2a). The extrapolation of the dashed lines in **a** and **c** to $T = 0$ demonstrates a violation of the Wiedemann-Franz law in a putative paramagnetic, non-Fermi-liquid ground state. This ground state is realized [22] exactly at the critical magnetic field B_c , *cf.* Fig. 1a. Error bars are derived from the standard deviation of the data in Fig. 2. **e**, Evolution of a shallow minimum in the isothermal ($0.1 \text{ K} \leq T \leq 0.3 \text{ K}$) $L(B)/L_0$ dependence. Data at lower T are not included because of the additional magnon heat transport at $B < B_c$ which will vanish as $T \rightarrow 0$. These minima are related to the $T^*(B)$ line of Fig. 1a, *cf.* the crossover fields (arrows) and widths (horizontal bars). Above $B^*(T) = B(T^*)$, L/L_0 values are consistent with L_{el}/L_0 values in Fig. S10 implying in the $T = 0$ limit $L/L_0 = 1$ at $B \neq B_c$ and an abrupt dip at $B = B_c$. Error bars as in **c** and **d**.

FIG. 4: **The evolution of the quasiparticle weights across a Kondo-breakdown quantum critical point.** Z_L , the quasiparticle residue at the generic part (away from the “hot spots”, *i.e.* the momenta that are connected by the AF ordering wavevector) and Z_S , the corresponding quasiparticle residue of the small Fermi surface, are nonzero on the two sides of the QCP, but each one approaches zero as the QCP is approached from the respective side. Also shown are the illustrations of the large and small Fermi surfaces, which refer to those with the f -electrons delocalized and localized, respectively. The actual Fermi surfaces in both cases are multi-sheeted, and can be located in the first Brillouin zone in a more complex way.

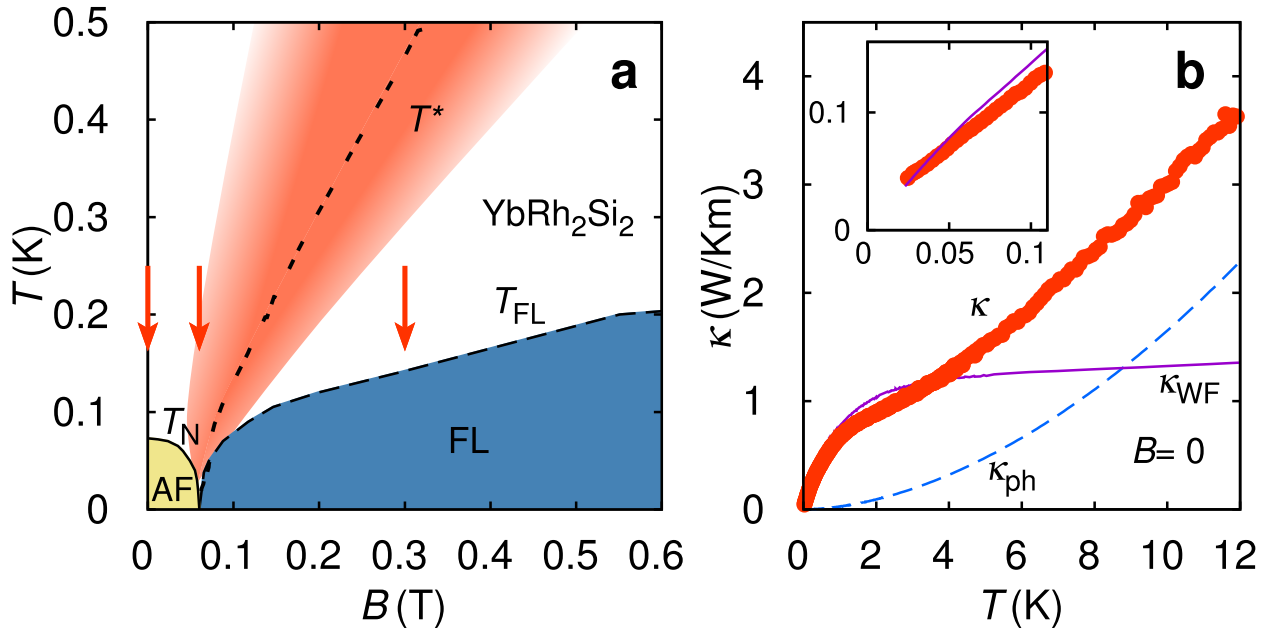


Figure 1

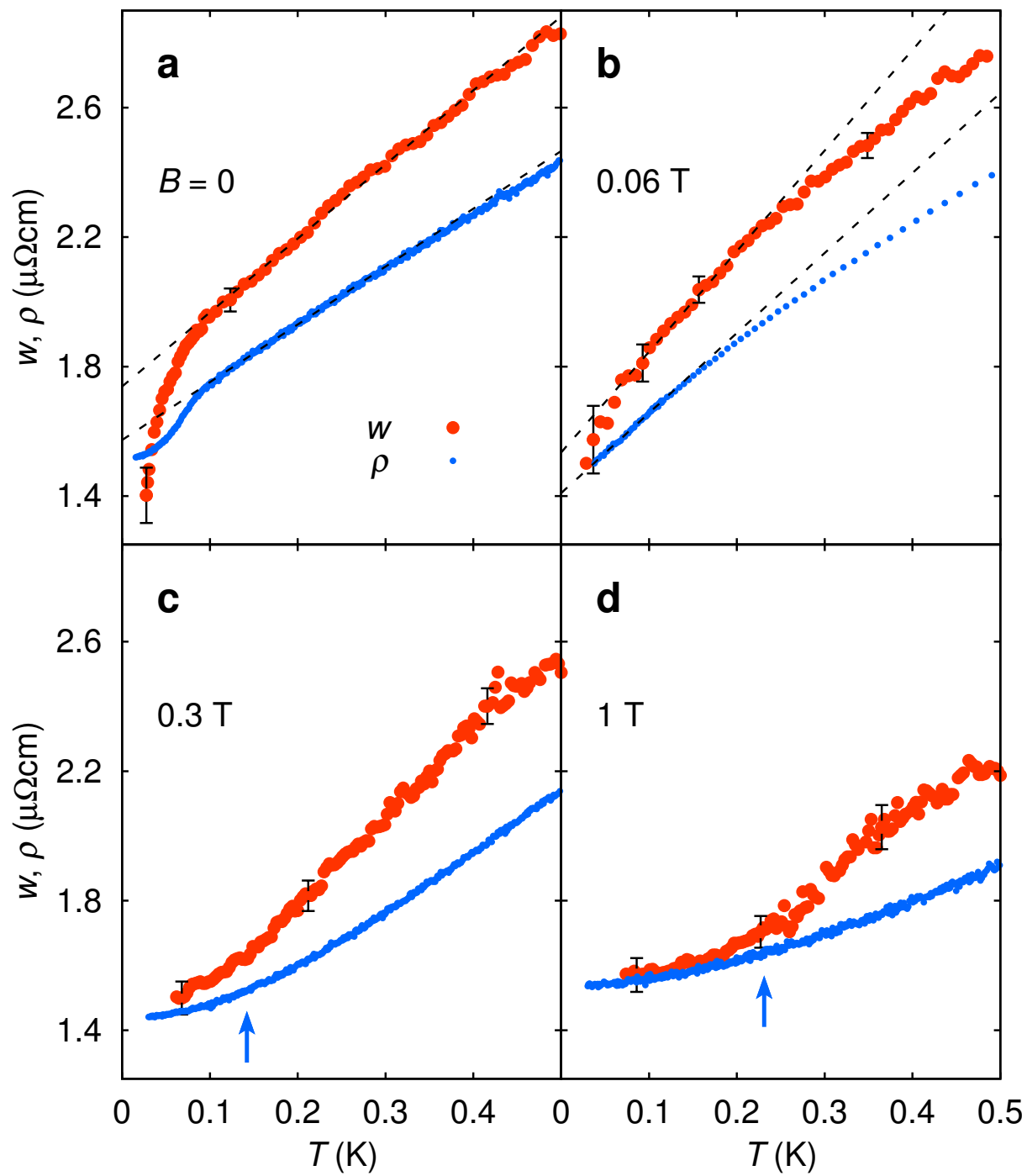


Figure 2

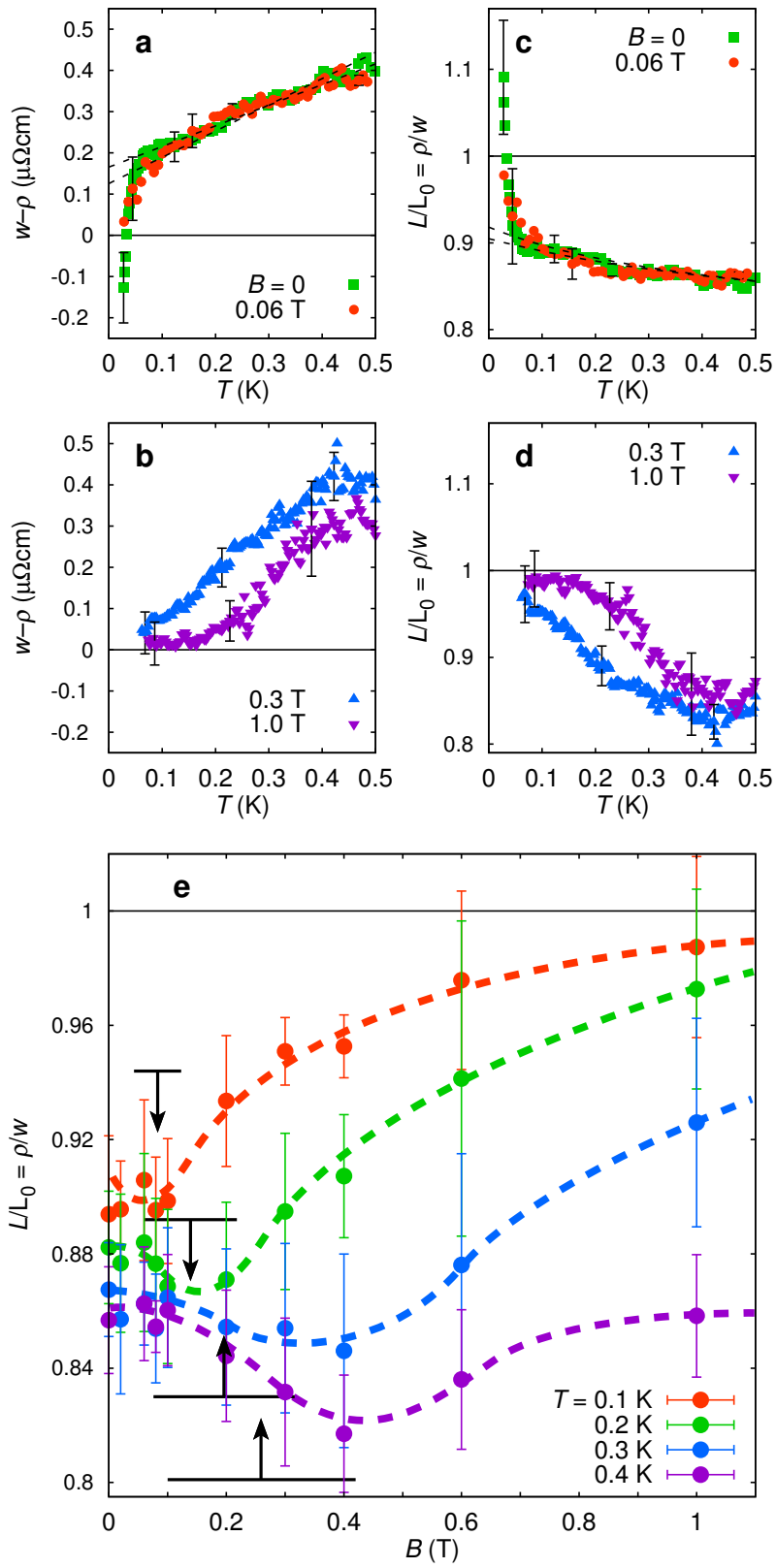


Figure 3

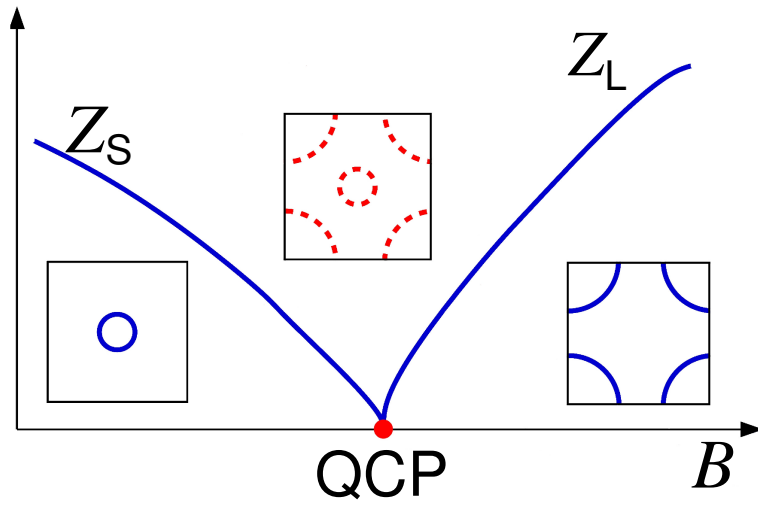


Figure 4

Supplementary Information for
“Thermal and Electrical Transport across a Magnetic
Quantum Critical Point”

I. BACKGROUND

The low-temperature behaviour of the heavy-fermion metal YbRh_2Si_2 was studied by means of thermal and electrical transport across its field-induced quantum critical point (QCP). The thermal conductivity of metals is typically measured down to temperatures in the Kelvin range. [1, 2] Because of the low energy scales, measurements in the heavy-fermion metals have been extended down to temperatures as low as 0.06 K (Ref. 3) or even 0.04 K (Ref. 4). In our case, special efforts have been made to measure the thermal conductivity at $B = 0$ and 0.02 T down to 0.025 K due to the very low Néel temperature $T_N = 0.07$ K (at $B = 0$). Furthermore, we have performed substantially more temperature scans for $B = 0$ in order to reduce the statistical error of the data. At $B = 0.06$ T, which is close to the critical field B_c , we were able to measure the thermal conductivity down to 0.04 K. At higher fields, the measurements of the thermal conductivity were performed down to 0.06 K.

II. CONTACTS

Previous thermal transport studies pointed out the strong influence of thermal contact resistances and demonstrated the necessity of a careful contact preparation.[3, 5] Subsequent to polishing the YbRh_2Si_2 sample (sample 1) for optimization of their geometry for our measurements, the sample surface was cleaned in an ultrasonic bath and rinsed in ethanol. The contact pads were prepared by evaporating a gold film (thickness of ≈ 50 nm) and applying a lift-off technique which allowed for optimum pad width and separation. Gold evaporation was conducted by using electron beam evaporators in ultra-high vacuum which turned out to provide superior contacts compared to thermal evaporation. Gold wires ($50 \mu\text{m}$) were then attached to the contact pads by silver paint to make use of the pad area. The silver paint covered an area of width of about $130 \mu\text{m}$, which is very small compared to the distance between the contacts (2.9 mm). This contributes to a systematic standard error of about 4.5% in the estimation of the geometry factor. It is the same for all experiments. We did not observe any indication of diminished thermal conductivity due to contact resistances down to 0.025 K. The same contacts were used for thermal and electrical conductivity measurements.

III. SYSTEMATIC ERRORS

Although most measurements were performed on a sample cut specifically for thermal transport, sample 1 ($4.2 \times 0.5 \times 0.1 \text{ mm}^3$), additional electrical resistivity measurements were done on a second sample (sample 2) with average size $1.7 \times 0.41 \times 0.06 \text{ mm}^3$ from the same piece of crystal. This was necessary to systematically study the dependency of the low- T electrical resistivity on the current, *cf.* Section IV. Because of the inhomogeneous thickness of the samples, the geometry factor could not be determined with very high precision. However, the measured resistivities could perfectly be rescaled by a factor 1.25 ± 0.03 and corrected by a difference in residual resistivity of $0.22 \mu\Omega\text{cm}$. The former number allows to estimate the uncertainty in the determination of the sample dimensions, *i.e.*, the systematic standard error for the geometry factor. It is about 2.5%, and it is the same for all measurements. The thermal and electrical transport coefficients were measured on the same sample (sample 1) with the same contact configuration, and the Lorenz ratio $L(T)/L_0 = \rho(T)/w(T)$ is affected by an additional systematic error of about 4.5% due to the finite width of the contacts, see Section II. Thus, a total systematic error of 7% has to be considered, *i.e.*, it will shift systematically all curves of Fig. 3 of the main text. This explains why in the region of the field-induced Fermi-liquid in the phase diagram, *e.g.*, at $B \geq 0.6 \text{ T}$ and below $T = 0.15 \text{ K}$, the difference $w(T) - \rho(T)$ is not exactly zero, and the Lorenz ratio does not reach exactly one.

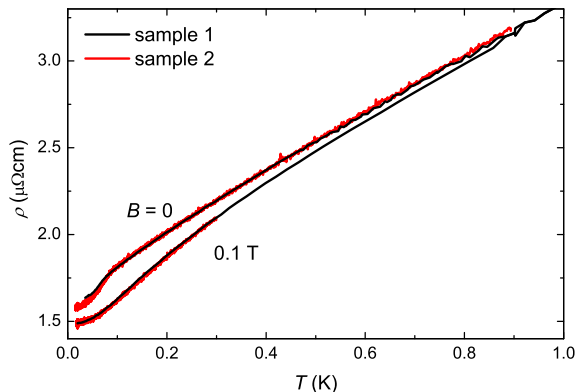


FIG. S1: Temperature dependency of the electrical resistivities of two YbRh_2Si_2 single crystals from the same batch. The data of sample 2 have been multiplied by a factor 1.25 ± 0.03 and corrected by a difference in residual resistivity of $0.22 \mu\Omega\text{cm}$.

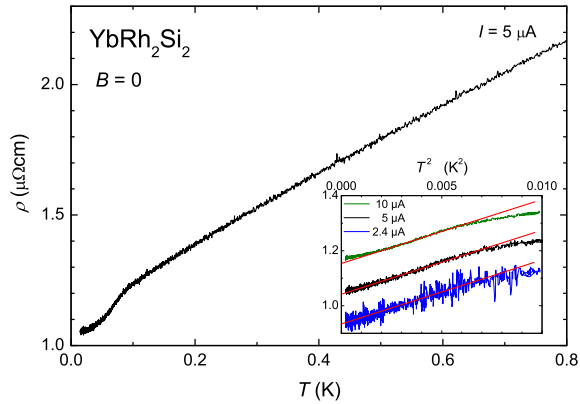


FIG. S2: Temperature dependency of the electrical resistivity of sample 2. The kink at about 0.07 K indicates the Néel temperature T_N . Below T_N a T^2 dependency of the resistivity is observed as expected [6] (*cf.* inset where the individual curves are shifted vertically).

IV. ELECTRICAL RESISTIVITY

The electrical resistivity $\rho(T)$ was determined by a four-point ac-technique in a ^3He - ^4He dilution refrigerator down to $T \approx 0.02$ K. Figure S1 shows the resistivity data of samples 1 and 2 at $B = 0$ and 0.1 T, respectively. The data for the second sample, which has a lower residual resistivity, have been scaled as described above. The data agree nicely, and we conclude that both samples show the same overall behaviour. The slightly larger resistivity in the zero-field curve below 0.05 K for sample 1 is due to heating effects. Therefore, the second sample was measured at different currents to investigate the influence of the current on the curvature of $\rho(T)$. The results below 0.1 K are displayed in the inset of Fig. S2 plotted as a function of T^2 , a temperature dependence expected below $T_N = 0.07$ K for $B = 0$ (Ref. 6). The heating effect can be neglected at a current of $5 \mu\text{A}$. We used the resistivity data with this current to evaluate the Lorenz ratio. As will be shown in a forthcoming paper, [7] the heating effect is particularly strong in the vicinity of B_c . In addition, it is increasing with increasing residual resistivity ρ_0 . For a single crystal of very high perfection with $\rho_0 \approx 0.5 \mu\Omega \text{ cm}$, no heating effect could be observed down to $T \approx 0.02$ K using a current of $50 \mu\text{A}$ (Ref. 8). In this case, $\Delta\rho \sim T$ was observed below $T = 0.1$ K down to the lowest accessible temperature of 0.02 K.

In all samples the magnetoresistivity was measured and compared to that of the samples investigated in Refs. 9, 10, to assure consistency of the properties observed in our samples

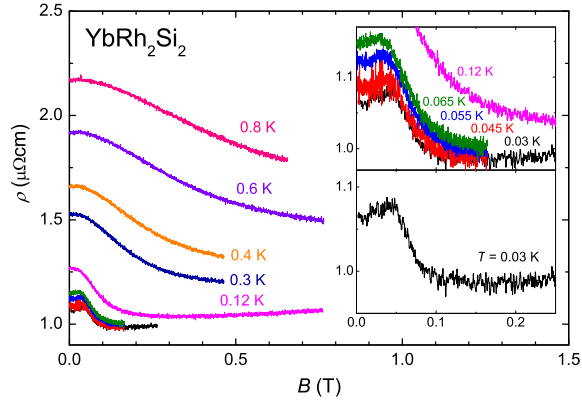


FIG. S3: Magnetoresistivity of sample 2 measured with a current of $5\mu\text{A}$. The upper inset magnifies the low field, low temperature region of the main panel to emphasize that the magnetoresistivity is positive inside the AF phase, but exhibits a rapid drop across a crossover field B^* . This is further illustrated in the lower inset for our lowest temperature $T = 0.03\text{ K}$. The rapid crossover across B^* was systematically analysed [9, 10]; in the zero-temperature limit, it corresponds to a sharp jump because the crossover width extrapolates to zero. The low-temperature data are also consistent with the existence of a peak in the residual resistivity as a secondary feature superimposed on the sharp jump, although its interpretation is not clearcut as it may also be associated with the Néel transition.

with those of the best single crystals grown so far. As an example, the magnetoresistivity of sample 2 is shown in Fig. S3: At $T = 0.03\text{ K}$ the change in resistivity associated with the crossover is about 10% (see insets of the same figure), as also found in the samples studied in Ref. 9 (*cf.* Fig. S5 of the Supporting Information of Ref. 9). The dominant feature is a rapid crossover across B^* , corresponding to a jump in the zero-temperature limit [9, 10]. The isothermal resistivity vs. the magnetic field at low temperatures are also consistent with the existence of a peak near B^* as a secondary feature superimposed on the sharp jump, although it could also be associated with the (classical) Néel transition.

V. THERMAL CONDUCTIVITY

A. Experimental details

The thermal conductivity $w(T)$ was measured using a steady-state two-thermometer, one-heater technique in a ^3He - ^4He dilution refrigerator down to $T \approx 0.025$ K. The heat loss along the wires and suspensions for thermometers and heater is estimated to be a factor of 1000 smaller than the heat flow through the sample. κ was calculated from the electrical power P released by a resistive heater, the temperature difference ΔT between two contacts on the sample and the geometry factor A as $\kappa = A \cdot P / \Delta T$. ΔT was measured by two RuO_2 resistance thermometers, that were calibrated against the primary (“cold finger”) sensor during each temperature run, using the resistances measured at zero heating power. A stability of better than 0.1 % of both sample temperature read-outs was achieved in the entire measurement range. For each stabilized bath temperature a set of four different heat currents was applied which results in temperature gradients $\Delta T / T = 1\% - 7\%$ along the sample. The proportionality between the applied heater power and the achieved temperature gradients at a constant bath temperature proves that the system is in the regime of linear response. The resulting raw data of κ were then averaged. Our measurement procedure implies the following uncertainties: i) The uncertainty in A represents a systematic error, that shifts all $\kappa(T)$ curves by a constant factor, as described in Section III; ii) the uncertainty in P is negligible because current and voltage at the heater can be measured with high accuracy; iii) the uncertainty in ΔT results from the measurement of the thermometer resistances and from errors in the calibration. Concerning the last point, two or more temperature runs have been performed at many fields, each with its own calibration. For a given field, the calculated $\kappa(T)$ values fall on top of each other within the scattering of the data. Therefore, the error in the calibration is negligible compared to the data scattering. In fact, the largest uncertainty arises from the measurement of the thermometer resistances due to the limited excitation current, especially at low T . It leads to scattering of the raw data and is significantly reduced in our final data by averaging over several points. As error bars we took the standard deviation of the raw data as displayed in Figs. 2 and 3 of the main text as well as Figs. S4 and S5. The systematic error due to the sample and contact geometry is not included, because it results only in a shift of all curves as explained in Section III. We

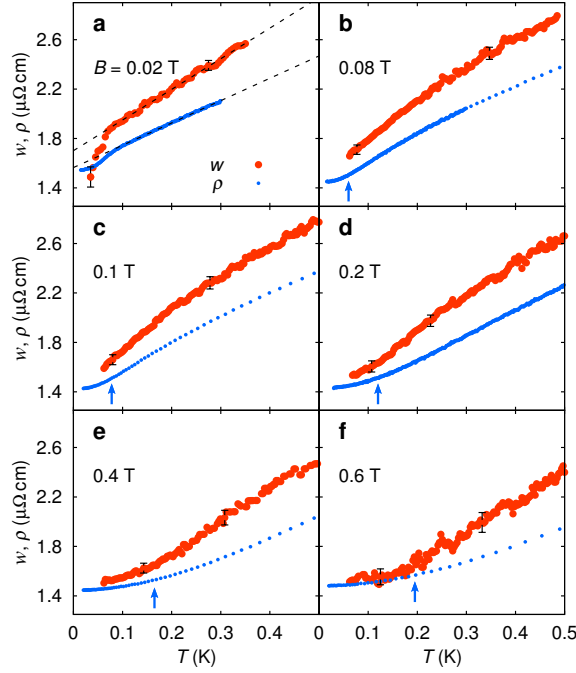


FIG. S4: Thermal and electrical resistivity $w = L_0T/\kappa_{el} \approx L_0T/\kappa$ and ρ plotted as a function of temperature, at $T \leq 0.5$ K for $B = 0.02$ T **a**, 0.08 T **b**, 0.1 T **c**, 0.2 T **d**, 0.4 T **e** and 0.6 T **f** ($B \perp c$). The arrows in **b** through **f** indicate the crossover to Fermi-liquid behaviour (*cf.* Fig. 1a of the main text). A significant drop is seen in the residual ($T \rightarrow 0$) thermal and electrical resistivities when going from $B = 0.02$ T **a** to 0.08 T **b** and 0.1 T **c**, which parallels the drop in the isothermal magnetoresistivity across B_c (*cf.* Fig. S3) as previously observed and attributed to an abrupt increase in the charge carrier concentration. [9, 10] Also, the slight rise of the residual thermal and electrical resistivities upon increasing field (*cf.* **d** through **f**) confirms the trend observed in Ref. 10 and ascribed there to the magnetoresistivity in the paramagnetic phase of YbRh_2Si_2 .

attribute the observation of w_0 being about 1% larger than ρ_0 in the Fermi liquid regime at high fields (Figs. 2d and S4f) to this systematic error.

Finally, the noise level in the data of the thermal resistivity increases substantially with increasing magnetic field, as can be directly seen in Fig. S4. It is presumably due to the vibrations of the set-up wires in magnetic fields. This is the main reason why we could not perform reliable measurements below 0.06 K at fields larger than 0.06 T.

B. Phonon contribution

The phonon contribution, $\kappa_{\text{ph}}(T)$, to the measured thermal conductivity $\kappa(T)$ can be separated from the electronic part, $\kappa_{\text{el}}(T)$, by avoiding the low-temperature range where a significant inelastic scattering of the charge carriers has been evidenced (*cf.* Fig. **1b** of the main text and Ref. 4).

After having subtracted $\kappa_{\text{el}}(T) = \kappa_{WF}(T) = L_0 T / \rho(T)$ from $\kappa(T)$ for $6 \text{ K} < T < 12 \text{ K}$, *i.e.*, assuming the validity of the Wiedemann-Franz (WF) law to hold in this temperature range for the electronic heat transport, the phonon contribution $\kappa_{\text{ph}}(T)$ is found to follow a T^ϵ dependence with $\epsilon = 2 \pm 0.2$. As shown in Fig. **1b**, main text, an extrapolation of this power law to lower temperatures indicates a negligible $\kappa_{\text{ph}}(T)$ below 1 K, *i.e.*, within the temperature range of interest in the present work. The uncertainty in the exponent has only little effect on the estimated $\kappa_{\text{ph}}(T)$ below 5 K. The insignificance of $\kappa_{\text{ph}}(T)$ below 1 K is further corroborated by the almost constant Lorenz ratio $L/L_0 \approx 0.86$ within the range $0.5 \text{ K} < T < 1 \text{ K}$, presumably associated with a measured thermal conductivity of purely electronic origin. Assuming this Lorenz ratio to extend to above 2 K, $\kappa_{\text{el}}(T) = L T / \rho(T)$ can easily be estimated. Subtracting this from the measured $\kappa(T)$, the phonon part is obtained once more. Below about 5 K, $\kappa_{\text{ph}}(T)$ obtained by the latter procedure is found to be in very good agreement with that from the former one.

We, therefore, conclude that below about 10 K, $\kappa_{\text{ph}}(T)$ of YbRh_2Si_2 follows a T^2 dependence, as commonly expected for a metal in this temperature range due to dominating phonon scattering from the conduction electrons. [11] A nearly T^2 -dependence of $\kappa_{\text{ph}}(T)$ has indeed been observed for several heavy-fermion compounds, e.g., CeB_6 , [12] CeNiSn [13] and CeAuAl_3 [14] in a similar temperature range. In these systems the dominant phonon wavelength, λ_{ph} , is assumed to be shorter than the mean free path of charge carriers, l_{el} , Ref. 15. This assumption, thus, appears to hold also for the YbRh_2Si_2 single crystal studied here. On the other hand, for CeCu_2Si_2 , [16] CeAl_3 [17] and CeCu_6 [18] $\kappa_{\text{ph}}(T)$ depends almost linearly on T , which hints at the opposite relation between λ_{ph} and l_{el} , *i.e.*, $\lambda_{\text{ph}} > l_{\text{el}}$, Ref. 15.

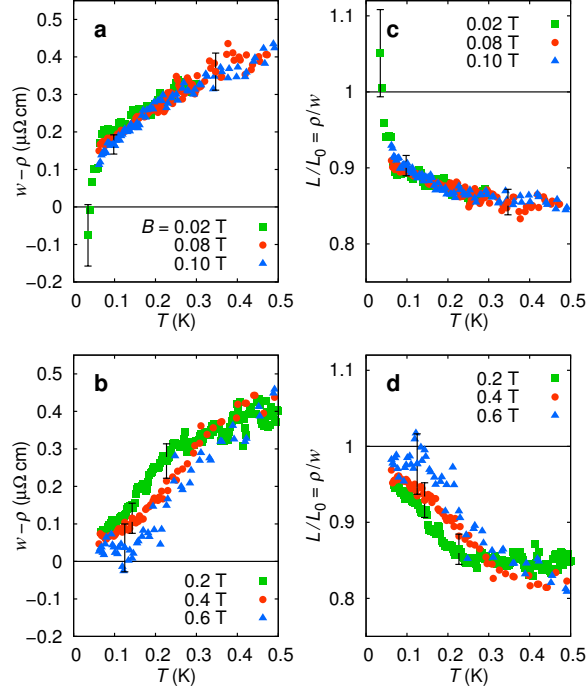


FIG. S5: Difference $(w - \rho)$ vs T at $B = 0.02$ T, 0.08 T and 0.1 T **a** as well as 0.2 T, 0.4 T and 0.6 T **b**. **c**, **d** Lorenz ratio $L/L_0 = \rho/w$ vs T for the same fields as in **a**, **b**. The data for $B = 0.02$ T are similar to those for $B = 0$ (*cf.* Figs. **3a** and **c** of the main text). They provide convincing evidence for an extra heat channel which adds to the one of the electronic quasiparticles and is most likely due to AF magnons (see text). For $B = 0.6$ T a Fermi-liquid phase forms below $T \approx 0.15$ K. This can also be anticipated for $B = 0.4$ T and 0.2 T and even for $B = 0.1$ T and 0.08 T at correspondingly lower crossover temperatures.

C. Electronic contribution

The thermal conductivity obtained by subtracting $\kappa_{\text{ph}}(T)$ from the measured $\kappa(T)$ is $\kappa_{\text{el}}(T)$. In Fig. S6 we show that the temperature coefficient, κ_{el}/T , increases logarithmically upon cooling from $T = 2$ K to about 0.3 K. A corresponding logarithmic divergence was observed also for the Sommerfeld coefficient of the electronic specific heat, $\gamma = C_{\text{el}}/T$, [19, 20] and the thermopower coefficient S/T . [21]

In the following, we are interested in the corresponding thermal resistivity $w(T) = L_0 T / \kappa_{\text{el}}(T)$, which is displayed together with $\rho(T)$, in Fig. 2 of the main text for four different fields. The results of $w(T)$ and $\rho(T)$ for other magnetic fields are shown in Fig. S4. The data taken at $B = 0.08$ T through 0.6 T are complementary to those at $B = 0.3$ T and

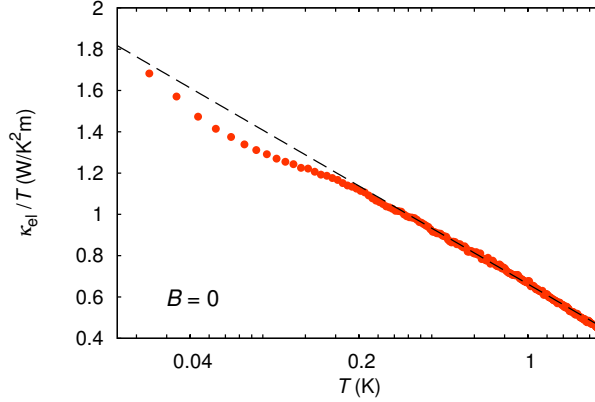


FIG. S 6: Temperature coefficient of the $B = 0$ electronic thermal conductivity, κ_{el}/T , of YbRh_2Si_2 plotted as a function of T on a logarithmic scale to emphasize that it follows a logarithmic behaviour on cooling from 2 K to about 0.3 K.

1 T presented in Figs. 2**c** and 2**d** of the main text. The data at $B = 0.02$ T are likewise complementary to those at zero field presented in Fig. 2**a** of the main text. Like in the zero-field case, they show a low-temperature downturn in the AF phase which contains the magnon contribution to the heat conduction. Figure S5 displays the difference $w(T) - \rho(T)$ **a,b** and the ratio $\rho(T)/w(T) = L/L_0$ **c,d** for the data shown in Fig. S4. The existence of a magnon contribution to the thermal conductivity at $B = 0.02$ T is indicated by $(w - \rho)$ being negative and L/L_0 being larger than one below $T \approx 0.03$ K, very similar to the results at $B = 0$ (*cf.* Figs. 3**a** and 3**c** of the main text). Within the experimental uncertainties, the data at $B = 0.6$ T indicate Fermi-liquid behaviour and the validity of the WF law below $T \approx 0.15$ K. Fermi-liquid behaviour below a crossover temperature which continuously decreases with decreasing magnetic field is inferred for both $B = 0.4$ T and 0.2 T **b,d**. This implies $L/L_0 \rightarrow 1$ as $T \rightarrow 0$, with which also the results obtained for $B = 0.1$ T and even 0.08 T are compatible **a,c**.

The data for w and ρ measured as a function of temperature for fixed magnetic fields, shown in Fig. 2 of the main text and Fig. S4, have been used to determine the isothermal Lorenz ratio as a function of field displayed in Fig. 3**e** of the main text. The isothermal field dependence exhibits a minimum near B^* . This striking behaviour is also seen in preliminary results obtained from direct isothermal measurements of w and ρ as a function of field in a sample with lower residual resistivity [22].

D. Magnon contribution

For the measurements performed at $B = 0$ (Fig. 2a, main text) as well as 0.02 T (Fig. S4a) a downturn in the thermal resistivity is found below $T \approx 0.1$ K and $T \approx 0.08$ K, respectively, while at $B = 0.06$ T a similar but smaller feature occurs below $T \approx 0.07$ K (Fig. 2b, main text). One may ascribe this drop in $w(T)$ to the freezing out of inelastic scatterings provided by spin fluctuations in the electronic heat transport. However, while ferromagnetic spin fluctuations remain unchanged, antiferromagnetic ones grow at sufficiently low temperatures and magnetic fields, as inferred from NMR Knight shift and spin-lattice relaxation rate measurements, respectively. [23] Therefore, the only natural interpretation of this drop involves heat carriers which add to the electronic ones. The existence of a corresponding excess contribution to the thermal conductivity, $\Delta\kappa(T)$, is proven by our observation that for $B = 0$ and $B = 0.02$ T the thermal resistivity becomes smaller than the electrical resistivity, *cf.* Figs. 2a and S4a. $\Delta\kappa(T)$ adds to $\kappa_{\text{el}}(T)$ which we assume to be given by L_0T/ρ at temperatures well below T_N , *i.e.*, we assume the Wiedemann-Franz law to describe the electronic transport in the Fermi-liquid phase well below T_N . The observed $\Delta\kappa(T)$ falls into the range $2 - 5 \cdot 10^{-3}$ W/Km between 0.025 and 0.03 K. Because this value of $\Delta\kappa$ is close to the experimental uncertainty, its temperature dependence is hard to be experimentally determined. Nevertheless, its existence has been confirmed by repeated measurements. Lattice vibrations are unapt to account for this extra thermal conductivity, as the largest expected κ_{ph} , which is limited by the sample dimension ($\approx 100 \mu\text{m}$) and, employing the lattice specific heat, [20] is estimated to be less than $1 \cdot 10^{-5}$ W/Km in this range.

Another potential thermal heat channel is that of AF magnons. The signature of these spin-wave excitations was clearly observed [20] in the zero-field specific heat examined down to $T = 0.018$ K for an YbRh_2Si_2 single crystal being of similar quality as samples 1 and 2. As seen in Fig. S7, below $T = 0.05$ K the specific heat can be described by $\Delta C = C - C_{\text{ph}} - C_{\text{Q}} = \gamma T + \beta T^3$, with C_{ph} and C_{Q} being, respectively, the phonon and the nuclear quadrupole contributions, $\gamma = 1.64$ J/(K²mol) and $\beta = 132.2$ J/(K⁴mol). The huge electronic contribution $C_{\text{el}} = \gamma T$ denotes a heavy Landau FL phase. [20] The Debye-like term $C_m \sim T^3$ is characteristic of the contribution of long-wavelength AF acoustic magnons. In the framework of the Debye theory and using the measured β value, we can estimate

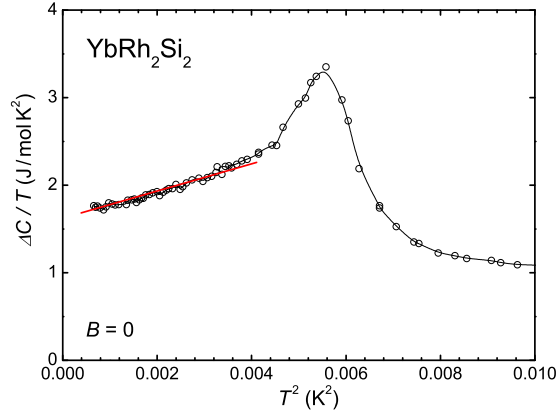


FIG. S7: Specific heat of YbRh_2Si_2 , shown as $\Delta C/T$ versus T^2 . $\Delta C(T) = C(T) - C_{\text{ph}}(T) - C_{\text{Q}}(T)$, where $C_{\text{ph}}/C_{\text{Q}}$ denotes the phonon/nuclear quadrupole contribution. The red line indicates a T^3 contribution to ΔC below 0.05 K. [20]

the “magnetic Debye temperature”, Θ_m , and the group velocity v_m of the magnons to be 4.2 K and 36 m/s, respectively. This Debye temperature corresponds to the AF exchange interaction suitably averaged over the three main spatial directions. The extracted group velocity is substantially smaller than that for typical Ce-based heavy-fermion AF metals, *e.g.*, about one-tenth of the corresponding value for CeAl_2 , [24] reflecting both the averaging over the spatial directions as well as the weak Néel order of YbRh_2Si_2 . The classical kinetic relation, $\kappa_m = (1/3)C_m v_m l_m$ (l_m : magnon mean free path), allows to estimate the magnon contribution to the thermal conductivity, κ_m . In order to obtain a κ_m of $2 - 5 \cdot 10^{-3}$ W/Km in the range 0.025 – 0.03 K as observed in Fig. 2a of the main text and Fig. S4a, the corresponding magnon mean free path l_m has to be in the range of 2 – 13 μm . Since in the low-temperature limit l_m is expected to be equal in size to that of the AF domains, the latter are estimated to be of the order of a few μm below about 0.03 K which, indeed, is a reasonable order of magnitude. [25]

The less pronounced downturn in $w(T)$ observed below $T = 0.07$ K at $B = 0.06$ T (Fig. 2b, main text) is ascribed to overdamped AF magnons, which were shown, via inelastic neutron scattering experiments, [26, 27] to exist for antiferromagnetically ordered materials substantially above the Néel temperature. Heat transport by short-lived magnon excitations has been reported, *e.g.*, for the parent compound of the 214 high- T_c cuprates, La_2CuO_4 , an $S = 1/2$, 2D antiferromagnet with a Néel temperature $T_N \approx 310$ K. [28] In particular, $S = 1$

chain systems, like Y_2BaNiO_5 (Ref. 29) and $\text{Ni}(\text{C}_2\text{H}_8\text{N}_2)_2\text{NO}_2(\text{ClO}_4)$ (NENP) (Ref. 30) have served as model systems in this context.

We would like to note that the magnon contribution cannot be avoided by performing thermal Hall measurements. In contrast to the case of phonons, [2] magnons may generate a transverse thermal gradient. [31]

VI. EXTRAPOLATION OF THE LORENZ RATIO TO ZERO TEMPERATURE IN QUANTUM CRITICAL SYSTEMS

We now discuss the various isofield and isothermal scans that are used for the extrapolation of the Lorenz ratio in the vicinity of a QCP. We will discuss the special case that is pertinent to YbRh_2Si_2 , namely a field-induced QCP separating an AF ordered phase and a paramagnetic Fermi-liquid phase.

Fig. S8a illustrates different temperature scans in different parts of the phase diagram. Scan A starts from the quantum critical regime, but runs into the ordered phase; by construction, it passes through the phase boundary. The zero-temperature limit of $w(T)$, $\rho(T)$ and $L(T)/L_0$ so extrapolated does not reflect the quantum critical behavior, but instead only captures that of the ordered phase. Scan B also starts from the quantum critical regime, but runs into the low-temperature paramagnetic Fermi liquid phase; it passes through a crossover temperature. Again, the zero-temperature limit so extrapolated does not reflect the quantum critical behavior, but instead only captures that of the paramagnetic Fermi liquid phase. Scan C starts from the quantum critical regime, and goes all the way to the QCP as the temperature is lowered. The zero-temperature limit so extrapolated captures the properties of the QCP. In practice, however, the same purpose can be achieved by carrying out scans C_1 or C_2 (provided there is enough dynamical range in temperature). These start in the quantum critical regime but stop before running into the Néel temperature or the crossover temperature to the paramagnetic Fermi liquid region. The zero-temperature limit so extrapolated also manifests the behavior of the QCP.

The different temperature scans will also be manifested in the isothermal properties of L/L_0 as a function of the control parameter, as illustrated in Fig. S8b. Scan a starts from the paramagnetic Fermi-liquid regime, and runs into the quantum critical regime. As it passes through the crossover scale between the two regimes, we expect to see a crossover in

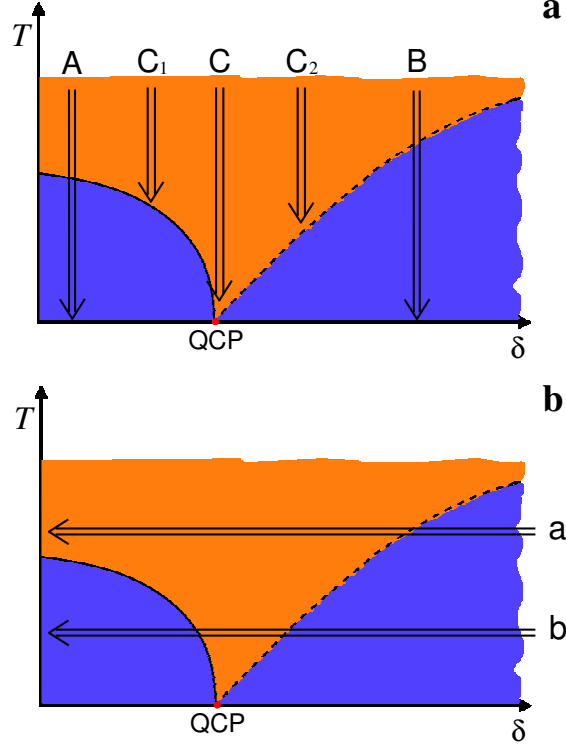


FIG. S8: Isofield **a** and isothermal **b** scans for the extrapolation of the Lorenz ratio in the vicinity of a QCP, as described in detail in the text.

L/L_0 in a way that compliments what is seen in the temperature scan B. Scan B starts from the paramagnetic Fermi-liquid regime, passing through the quantum critical regime, and runs into the ordered phase. Because it passes through both the crossover temperature and the Néel temperature lines, this isothermal scan will reflect the features of both temperature scan B and temperature scan A.

In this work, our primary focus is on temperature scans C_1 (Figs. 2a, 3a, 3c), scans close to C (Fig. 2b), and scans C_2 (*e.g.* Figs. S4b and c) through B (Figs. 2c, 2d, 3b, 3d). In addition, isothermal scans a (Fig. 3e) are conducted. Because of the masking effect of magnons on the electronic heat transport, we do not attempt to analyze any scan b. Temperature scans A cannot be performed in YbRh_2Si_2 because of the small value of the critical field B_c .

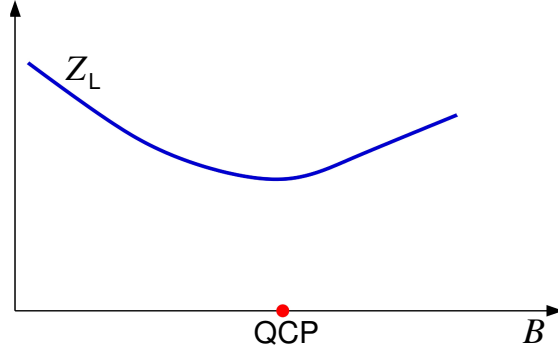


FIG. S9: The evolution of the quasiparticle weights across a heavy-fermion spin-density-wave quantum critical points. Z_L of the large Fermi surface stays nonzero as the system is tuned through the QCP.

VII. THEORETICAL ASPECTS

The validity of the WF law in the vicinity of a heavy-fermion spin-density-wave QCP was briefly discussed in the main text. Across such a QCP, the heavy quasiparticles remain intact in the main part of the Fermi surface. In these “cold” regions, the quasiparticles do not experience scattering by the AF spin fluctuations, and their spectral weight—the quasiparticle residue Z —stays finite as the control parameter moves through the QCP (Fig. S9). L/L_0 must be equal to one in this case. Even the contributions from the “hot” regions, which experience scatterings by the bosonic collective fluctuations, cannot violate the WF law, as was illustrated by the case of ZrZn_2 (Ref. 1) where ferromagnetic fluctuations influence the entire Fermi surface.

This is in contrast to the Kondo-destroying local quantum critical description which is illustrated in Fig. 4 of the main text. In the paramagnetic Fermi-liquid state, the conduction electron self-energy, $\Sigma(\mathbf{k}, \omega, T)$ contains a pole at the Kondo-resonance energy. It converts the f -moments into a part of the Landau quasiparticles, thereby creating a large Fermi surface. The quasiparticle residue at the large Fermi momenta, \mathbf{k}_F^L , is nonzero, $Z_L(\mathbf{k}_F^L, \omega = 0, T = 0) \neq 0$. In the AF Fermi-liquid state, the Kondo resonance is destroyed. The Fermi surface is given by that of the conduction electrons only in the presence of a staggered magnetic field. Away from the “hot spots”, there are Landau quasiparticles associated with a small Fermi surface. The quasiparticle residue at such generic small Fermi momenta, \mathbf{k}_F^S , is nonzero, $Z_S(\mathbf{k}_F^S, \omega = 0, T = 0) \neq 0$.

In these Fermi-liquid regimes, both the electrical and electronic heat currents are predominantly carried by Landau quasiparticles. At nonzero temperatures, the electronic heat carriers experience inelastic scatterings. Because the non-Umklapp processes are considerably more efficient in relaxing electronic heat current than electrical current, even in anisotropic systems at low temperatures, the electron-electron scatterings lead to an electronic Lorenz ratio $L_{\text{el}}/L_0 < 1$ at nonzero temperatures. [32] The effect is similar to the usual case of electron-phonon scattering. [11] The Umklapp scatterings are expected to contribute equally efficiently to the thermal and electrical resistivities. In the zero-temperature limit, well-defined quasiparticles remain, but the inelastic scatterers are frozen out; only the elastic scattering processes remain, and L_{el}/L_0 is equal to 1. This is illustrated in Fig. S10, where L_{el}/L_0 reaches 1 as the system moves away from the QCP (at B_c) into the Fermi-liquid regimes on both sides.

In the quantum critical regime, low-energy electronic excitations occur at both the small and large Fermi surfaces (Fig. 4, main text). The single-electron self-energy at both \mathbf{k}_F^S and \mathbf{k}_F^L vanishes at the $\omega = 0$ and $T = 0$ limit, but has the scaling form as a function of ω and T as given in Eq. 1 (main text). This reflects the fluctuations of the Fermi surfaces, which characterize the quantum fluctuations in the *entire* quantum critical regime. We will consider the electrical and heat currents carried by the electronic excitations at both \mathbf{k}_F^S and \mathbf{k}_F^L , all of which are non-Fermi liquid in nature as specified by Eq. 1. These electronic current carriers are subject to inelastic scatterings that are associated with the quantum criticality. While such scattering processes are many-body in nature, they can still be divided into Umklapp

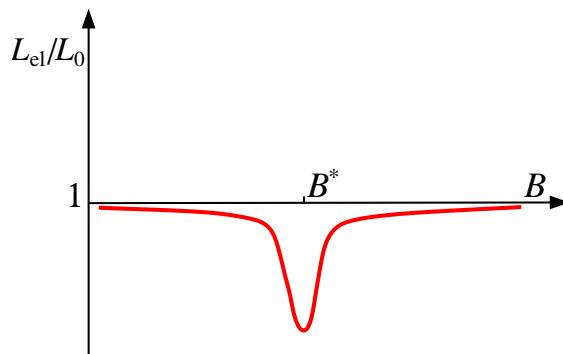


FIG. S10: Expected isothermal behaviour of the Lorenz ratio across a Kondo-destroying QCP. $B^*(T) = B(T^*)$ is the Kondo breakdown scale at a nonzero but small T . At zero temperature an abrupt dip occurs at $B^* = B_c$

and non-Umklapp processes. The non-Umklapp processes will contribute considerably more to the thermal resistivity than to the electrical resistivity. As a result, L_{el}/L_0 will be less than 1.

The end result is a dip of L_{el}/L_0 near B_c . Fig. S10 illustrates the corresponding isothermal behaviour of L_{el}/L_0 for a given nonzero but low T , where the dip is expected to be centered at $B^*(T) = B(T^*)$, cf. Fig 1a of the main text. As $T \rightarrow 0$, the dip becomes abrupt at B_c .

-
- [1] Smith, R. P. *et al.* Marginal breakdown of the Fermi-liquid state on the border of metallic ferromagnetism. *Nature* **455**, 1220-1223 (2008).
 - [2] Wakeham, N. *et al.* Gross violation of the Wiedemann-Franz law in a quasi-one-dimensional conductor. *Nature Commun.* **2**, 396–401 (2011).
 - [3] Tanatar, M. A., Paglione, J., Petrovic, C. & Taillefer, L. Anisotropic violation of the Wiedemann-Franz law at a quantum critical point. *Science* **316**, 1320-1322 (2007).
 - [4] Tomokuni, K. *et al.* Thermal transport properties and quantum criticality of heavy fermion YbRh_2Si_2 . *J. Phys. Soc. Jpn.* **80**, Supplement A SA096 (2011).
 - [5] Seyfarth, G. *et al.* Multiband superconductivity in the heavy fermion compound $\text{PrOs}_4\text{Sb}_{12}$. *Phys. Rev. Lett.* **95**, 107004 (2005).
 - [6] Gegenwart, P. *et al.* Magnetic-field induced quantum critical point in YbRh_2Si_2 . *Phys. Rev. Lett.* **89**, 056402 (2002).
 - [7] Lausberg, S. *et al.*, to be published (2012).
 - [8] Westerkamp, T. Quantenphasenübergänge in den Schwere-Fermionen-Systemen $\text{Yb}(\text{Rh}_{1-x}\text{M}_x)_2\text{Si}_2$ und $\text{CePd}_{1-x}\text{Rh}_x$. PhD Thesis (TU Dresden, 2008).
 - [9] Friedemann, S. *et al.* Fermi-surface collapse and dynamical scaling near a quantum critical point. *Proc. Natl. Acad. Sci. USA* **107**, 14547-14551 (2010).
 - [10] Friedemann, S. *et al.* Discontinuous Hall coefficient at the quantum critical point in YbRh_2Si_2 . *J. Phys.: Condens. Matter* **23**, 094216 (2011).
 - [11] Ziman, J. M. Electron and phonons *Clarendon Press* (1960).
 - [12] Peysson, Y. *et al.* Thermal properties of CeB_6 and LaB_6 . *J. Magn. Magn. Mat.* **47–48**, 63–65 (1985)
 - [13] Kitagawa, J. *et al.* Effects of valence fluctuation and pseudogap formation on phonon thermal

- conductivity of Ce-based compounds with ϵ -TiNiSi-type structure. *Phys. Rev. B* **66**, 224304 (2002).
- [14] Aoki, Y. *et al.* Thermal conductivity of CeAuAl₃ : Evidence of phonon scattering by Ce magnetic moment fluctuations. *Phys. Rev. B* **62**, 87–90 (2000).
- [15] Zimmerman, J. E. Low-temperature lattice heat conduction in high-resistivity alloys. *J. Phys. Chem. Sol.* **11**, 299–302 (1959).
- [16] Franz, W., Griebel, A., Steglich, F. & Wohlleben, D. Transport properties of LaCu₂Si₂ and CeCu₂Si₂ between 1.5 K and 300 K. *Z. Phys. B* **31**, 7–17 (1978).
- [17] Ott, H. R., Marti, O. & Hulliger, F. Low temperature thermal conductivity of CeAl₃. *Solid State Commun.* **49**, 1129–1131 (1984).
- [18] Peysson, Y., Salce, B., Ayache, C. & Bauer, E. Thermal conductivity of CeCu₆ and LaCu₆. *J. Magn. Magn. Mat.* **54–57**, 423–424 (1986)
- [19] Trovarelli, O. *et al.* YbRh₂Si₂: Pronounced non-Fermi-liquid effects above a low-lying magnetic phase transition. *Phys. Rev. Lett.* **85**, 626–629 (2000).
- [20] Custers, J. *et al.* The break-up of heavy electrons at a quantum critical point. *Nature* **424**, 524–527 (2003).
- [21] Hartmann, S. *et al.* Thermopower evidence for an abrupt Fermi surface change at the quantum critical point of YbRh₂Si₂. *Phys. Rev. Lett.* **104**, 096401 (2010).
- [22] Pfau, H. *et al.*, to be published (2012).
- [23] Ishida, K. *et al.* YbRh₂Si₂: Spin fluctuations in the vicinity of a quantum critical point at low magnetic field. *Phys. Rev. Lett.* **89**, 107202 (2002).
- [24] Bredl, C. D., Steglich, F. & Schotte, K. D. Specific heat of concentrated Kondo systems: (La,Ce)Al₂ and CeAl₂. *Z. Phys. B* **29**, 327–340 (1978).
- [25] For example, the AF domain size is roughly 16 μm for elemental chromium (Werner, S. A. *et al.*, *Phys. Rev.* **155**, 528–539 (1967)), and is $\approx 1\mu\text{m}$ for the $5f$ -based heavy-fermion compound UPt₃ (de Visser, A. *et al.*, *J. Magn. Magn. Mat.* **177**, 287–291 (1998)).
- [26] Wiltshire, M. C. K. & Elcombe, M. M. Temperature dependence of magnons in γ -MnCu. *J. Magn. Magn. Mat.* **31–34**, 127–128 (1983).
- [27] Wiltshire, M. C. K., Elcombe, M. M. & Howard, C. J. Temperature dependence of the magnetic excitations in γ -Mn₉₀Cu₁₀. *J. Phys. F: Met. Phys.* **15**, 1595–1611 (1983).
- [28] Hess, C. *et al.* Magnon heat transport in doped La₂CuO₄. *Phys. Rev. Lett.* **90**, 197002 (2003).

- [29] Kordonis, K. *et al.* Spin thermal conductivity of the Haldane chain compound Y_2BaNiO_5 . *Phys. Rev. Lett.* **97**, 115901 (2005).
- [30] Sologubenko, A. V. *et al.* Field-dependent thermal transport in the Haldane chain compound NENP. *Phys. Rev. Lett.* **100**, 137202 (2008).
- [31] Onose, Y. *et al.* Observation of the magnon Hall effect. *Science* **329**, 297 (2010).
- [32] Herring, C. *et al.* Simple property of electron-electron collisions in transition metals. *Phys. Rev. Lett.* **19**, 167 (1967).